Earth and Space Science

RESEARCH ARTICLE
10.1029/2020EA001099

Special Section:
A NEW ERA OF LIGHTNING OBSERVATIONS FROM SPACE

Comparison of Lightning Detection Between the FY-4A Lightning Mapping Imager and the ISS Lightning Imaging Sensor

Xiang Ni[1,2], Wen Hui[3], Qinghong Zhang[2], Fuxiang Huang[3], and Chuntao Liu[4]

[1]Chongqing Jinfo Mountain Karst Ecosystem National Observation and Research Station, Southwest University, Chongqing, China, [2]Department of Atmospheric and Oceanic Sciences, School of Physics, Peking University, Beijing, China, [3]National Satellite Meteorological Center, China Meteorological Administration, Beijing, China, [4]Department of Physical and Environmental Sciences, Texas A&M University at Corpus Christi, Corpus Christi, TX, USA

Key Points:

- Analysis of one-year lightning events of Lightning Mapping Imager (LMI) shows reasonable results such as, spatial distributions, diurnal cycle of radiances, and so on
- The diurnal cycle of an LMI lightning event could be adjusted to be close to the results of Lightning Imaging Sensor (LIS), suggesting further algorithm improvement
- Detection efficiency relative to International Space Station-LIS shows regional differences and well performance in capturing lighting activity at storm-scale

Correspondence to:
Q. Zhang,
qzhang@pku.edu.cn

Citation:
Ni, X., Hui, W., Zhang, Q., Huang, F., & Liu, C. (2021). Comparison of lightning detection between the FY-4A Lightning Mapping Imager and the ISS Lightning Imaging Sensor. *Earth and Space Science*, *8*, e2020EA001099. https://doi.org/10.1029/2020EA001099

Received 17 JAN 2020
Accepted 3 MAY 2021

Abstract The Lightning Mapping Imager (LMI) onboard Fengyun-4A (FY-4A) is the first Chinese lightning detection sensor in geostationary orbit. This study presents the lightning characteristics observed by the FY-4A LMI in its first year, and then observations from the Lightning Imaging Sensor (LIS) onboard the International Space Station (ISS) are used to validate the performance of the LMI sensor. LMI lightning events are defined by the pixel's luminosity exceeding the threshold radiance. During the first year of operation, LMI events revealed a reasonable geographical distribution. The diurnal cycles of LMI event/background/threshold radiance are in general agreement with the later afternoon peaks in previous findings. However, the LMI events that occurred around the LIS flash time and in the LMI observation field-of-view show a slightly delayed peak at around 1900 LST. This peak can be shifted closer to LIS's results after removing LMI events with event radiance lower than 300 $\mu J\ sr^{-1}\ m^{-2}\ \mu m^{-1}$, suggesting that a larger threshold radiance value is needed to qualify some of these LMI events. Finally, LIS lightning groups were matched with LMI lightning events using different temporal and spatial collocation criteria. The detection efficiency is defined by the fraction of LIS groups detected by LMI to assess LMI's performance. The LMI detection efficiency relative to LIS was found to be regionally dependent and lower in the daytime than at nighttime. These results contribute to applications of LMI lightning observations in storm research and provide suggestions for further algorithm improvement.

1. Introduction

Lightning observation from space is a key for better understanding and predicting high impact weather events. On the global scale, lightning observation from space dates back to the 1970s, when midnight lightning was photographed over a period of one year by the scanner onboard the block 5D series F1 satellite (Orville & Henderson, 1986). The long-term observation of lightning was initiated with the launch of the optical transient detector (OTD) in 1995. The OTD detected total lightning from a 735-km altitude and a 70° inclination orbit, with a ground resolution range from 8 km at nadir to about 20 km at the array corners (Boccippio et al., 2000). The OTD was the first spaceborne lightning sensor to provide a detailed and accurate lightning climatology at a global scale (Christian et al., 2003). As a successor of the OTD, the lightning imaging sensor (LIS) onboard the tropical rainfall measuring mission (TRMM; Kummerow et al., 1998) has monitored global lightning activity since 1998. The observation of TRMM-LIS span 17+ years, and a large amount of lightning data were collected. The long-term observations of these two sensors have initiated research efforts into the characteristics of lightning and its relationship to convection (Albrecht et al., 2016; Cecil et al., 2014; Chronis & Koshak, 2017; Liu et al., 2012; Petersen et al., 2005).

A flight spare of the TRMM-LIS was mounted on the International Space Station (ISS) in February, 2017 (known as ISS-LIS but referred to in this paper simply as LIS). The 3-year mission was extended by NASA to at least 2023. To date, LIS has served beyond its 3-year time frame. Blakeslee and Koshak (2016) introduced the instrument parameters of LIS, and a 3-year assessment of LIS observations suggest its detection efficiency is around 60% (Blakeslee et al., 2020). LIS is the same as its predecessor TRMM-LIS except that the LIS extends its observations to 54° owing to the high inclination orbit of ISS (51.6°). As such, LIS provides information on lightning climatology in regions outside of the observation scope of TRMM (38°) (Buechler et al., 2019). The basic mission of LIS is to extend the fundamental monitoring of lightning from space after

TRMM-LIS. Another contribution of LIS is that it will work as the "calibration standard" to assess and compare the performance of lightning observations from different geostationary satellites and anchor all observations to construct a global lightning data set.

OTD, TRMM-LIS, and ISS-LIS have been widely used in lightning climatology and severe convection research. However, these three sensors cannot monitor lightning on a continuous basis. To overcome this shortcoming, the optimal choice is to transfer the lightning sensor to a geostationary platform. Meanwhile, conventional observations on geostationary satellites, such as the brightness temperature from visible and infrared channels, are not directly related to convection intensity. On the contrary, the total lightning flash rate (intracloud rates + cloud-to-ground rates) is a good indicator of convective intensity as the cloud-to-ground flash rate alone was found to not be a reliable indicator of the convective vigor of storm severity (Cecil et al., 2005; Liu et al., 2012; MacGorman et al., 1988; Petersen et al., 2005). Moreover, studies have demonstrated a sudden increase in the total lightning flash rate (referred to as lightning jumps) before the outbreak of severe weather (Curtis et al., 2018; Farnell et al., 2017; NOAA-NASA, 2019; Rudlosky, Goodman, & Virts, 2019; Schultz et al., 2009; Williams et al., 1999). Observing lightning from a geostationary platform was proposed in the 1980s (Christian et al., 1989). The geostationary lightning mapper (GLM) is aboard the geostationary operational environmental satellite-R series (GOES-R, United States) satellite (Goodman et al., 2013; NOAA-NASA, 2019). In China, geostationary lightning sensor designs have been underway since before the launch of the lightning mapping imager (LMI) (Cao, 2016) onboard Fengyun-4A (FY-4A). With continuous lightning observations from geostationary satellites, it is possible to improve the lead time for severe weather warnings.

However, lightning detection sensors onboard geostationary satellites have only recently been put into operation. The first GLM was successfully launched on November 19, 2016, onboard the first satellite in the GOES-R Series (GOES-16, now the operational GOES-East satellite centered at 75.2°W). The second GLM was launched on March 1, 2018 (GOES-17, now the operational GOES-West satellite centered at 137.2°W). These two GLMs conduct full-disk observations and monitor the Western Hemisphere from 150°E to east 0°W, covering most of the Pacific Ocean, Atlantic Ocean, and the American continents. The first Chinese spaceborne optical lightning sensor, LMI, was mounted on the new-generation Chinese geostationary meteorological satellite FY-4A (Yang et al., 2017), which was launched on 11 December 2016. LMI has been used routinely for severe weather monitoring since early 2017. The European Meteosat Third Generation (MTG) Lightning Imager (LI) is scheduled for launch in 2021. Four LI sensors will monitor storms in Europe and Africa in the period from 2021 to 2041 (Dobber & Kox, 2016).

Researchers are increasingly turning to the geostationary lightning observation data for their weather analyses and predictions. Through case studies and qualitative research, Liang et al. (2017) revealed the ability of LMI to detect lightning events with different intensity in both the Northern Hemisphere and the Southern Hemisphere. Using the LMI lightning data, Cao et al. (2018) confirmed that intracloud lightning occurs earlier than cloud-to-ground lightning in the development stage, and that intracloud lightning occurs during all stages of convection. Applying the two-sigma lightning jump algorithm to GLM, Curtis et al. (2018) identified 15 of 25 GLM jumps that were accompanied by an increase in the radar intensity. The relationship between intensity variation and convective evolution was investigated in hurricanes with GLM's total lightning observation (Fierro et al., 2018). Further, the observations of GLM have been used in research on the microphysical characteristics of hurricanes (Hu et al., 2020) and short-term forecasts of convections (Fierro et al., 2019; Kong et al., 2020). However, before the GLM or LMI data can be applied, it is important to assess the associated lightning detection performance of the sensor. For example, Curtis et al. (2018) concluded that GLM's detection efficiency is between 70% and 90% and Zhang and Cummins (2020) found the detection efficiency was the highest during nighttime hours. By calculating the detection efficiency and false alarm rate, Bateman and Mach (2020) also confirmed that the detection efficiency of GLM could be better than 70% across the whole field-of-view. Field campaigns have also been conducted in the United States to collect the data for GLM validation (Padula et al., 2017). Liu et al. (2019) compared LMI with ground lightning and found differences in the seasonal variation and day-to-night ratio. In the present study, we assessed the performance of LMI in the first year for future applications.

Several approaches have been applied to validate satellite-based lightning sensors. Thompson et al. (2014) validated LIS with the World Wide Lightning Location Network and the Earth Networks Total Lightning

10.1029/2020EA001099

Network. Buechler et al. (2018) used an artificial laser pulse to validate the predicted GLM geolocation accuracy. These approaches have generally used ground observations to validate the lightning observations from space-borne satellites. An alternative approach is to conduct cross-validation between a well-characterized low-orbit sensor (i.e., the LIS) and a geostationary optical lightning instrument such as the GLM. Blakeslee et al. (2020) used GLM and ground-based lightning networks to independently validate the detection accuracy of LIS. The FY-4A LMI can therefore be validated using a similar approach with the known performance of ISS-LIS. The advantage of this method is that the observation principles of the sensors are the same. Because ground-based total lightning observations are sparse and not easy to obtain within the region covered by LMI, comparing the lightning detection from a low-orbit sensor and geostationary sensors provides an option that could help validate different lightning sensors and anchor the data to build a global lightning climatology data set.

The goal of this paper is to present the lightning characteristics observed from the FY-4A LMI during its first year in operation and to utilize LIS observations to validate the performance of the LMI sensor. The data and methods are introduced in Section 2. Lightning characteristics, such as the diurnal cycle and radiance criteria for lightning detection, are evaluated in Section 3. LMI performance is examined and compared to that of LIS in Section 4. Finally, a discussion and conclusions are presented in Section 5.

2. Data and Methods

Spaceborne lightning observations have been conducted for decades (Christian et al., 2003; Kummerow et al., 1998). Standard algorithms have been developed to process pixel observations from optical sensors such as OTD/LIS (Goodman et al., 2012); Goodman et al. (2012) describes the GLM algorithm in details. In principle, the LMI algorithms are similar to those of GLM.

Here, the concepts of LMI lightning detection algorithms are discussed in details, to lay a foundation for subsequent context. For each pixel (~7.8 km resolution at nadir), the observation is the radiance at 777.4 nm (Liang et al., 2017), which corresponds to the 777.4 nm line from the excited atomic oxygen. Due to the optical characteristics of lightning, this channel may include radiance from other sources (e.g., solar radiance and that from the Earth's surface). To separate lightning flash radiance from other types, the background radiance is assessed from a certain number (e.g., six according to Liang et al., 2017) of the most recent radiance values, which are recorded at a sample rate of 2 ms. The background radiance is then subtracted from the current pixel radiance to obtain the difference signal. This difference signal is influenced by noise and occasionally peaks during the lightning discharge. Therefore, threshold radiance is defined to determine whether the peak is caused by lightning. Obviously, the threshold radiance is also influenced by the solar background and is higher in the daytime. Finally, if the difference in radiance is larger than the threshold radiance, then the pixel is defined as an event, and the *difference* in radiance is considered as the event radiance. The event identification process is conducted in real time at the satellite. Once a lightning event is identified, the event information including radiance, time, location, pixel ID, and so on, is transmitted to the ground. The lightning flash event defined at each pixel is the basic unit for LMI observation and its physical concept is different from the pulse or stroke, as referred to by ground lightning observations.

The transmitted pixel-level observations from the space segment are first filtered in the pre-process system to identify those lightning events that stand out from the background and threshold radiance values, and to remove signal noise, such as solar glint, saturation and so on. The output of the pre-process system is the Level-1 lightning event data, which are used in this research. The Level-1 lightning event is then imported into the cluster algorithm. In the cluster algorithm, each integration period (2 ms) or one image frame often consists of more than one lightning event. If these multiple events are adjacent, they are defined as a lightning group. The group is defined in a single frame and does not indicate the temporal evolution of a lightning discharge process. Then, a lightning flash is defined as the set of groups that meet certain spatial and temporal thresholds. The lightning flash could range from one group with one event or multiple groups with many events. In addition, the lightning event, group, and flash all contain information, including the location and radiance. The clustering algorithms of FY-4A LMI are similar to the description above; further details are given in Liang et al. (2017).

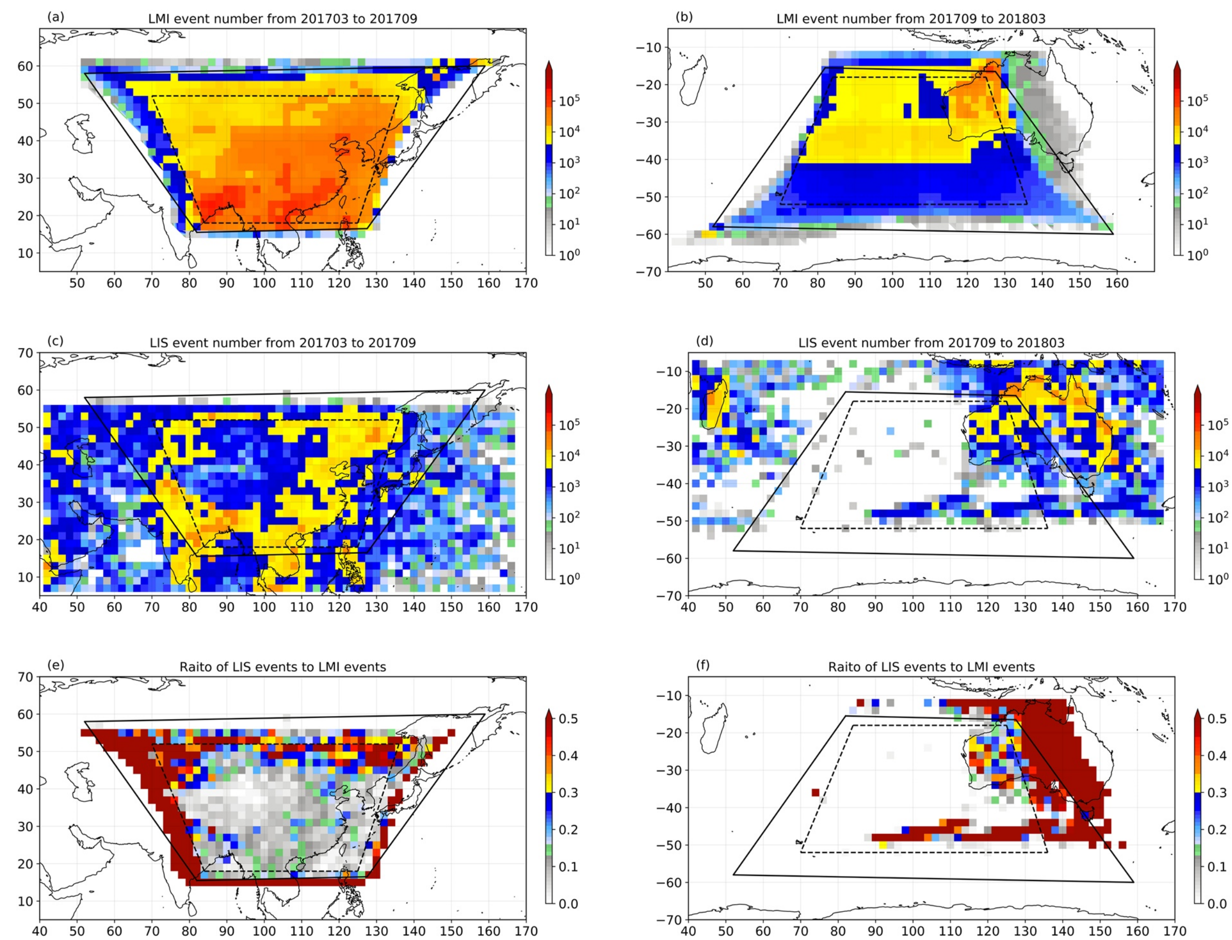

Figure 1. Populations of (a, b) Lightning Mapping Imager (LMI) events and (c, d) Lightning Imaging Sensor (LIS) events in both hemispheres. The ratio of LIS events to LMI events (e, f). The LMI events that occurred one minute before or after the LIS flash time and in the whole region were selected and counted in (a and b). The four corners connected with black lines are the reference points of the LMI observation field-of-view, and the regions surrounded by dashed lines are the regions used in the discussion.

Two sets of lightning observations are used in this study. The reference lightning data are the non-quality controlled ISS-LIS science data, which are used to assess LMI's lightning observations; these data are available from the website of the Global Hydrology Resource Center (https://ghrc.nsstc.nasa.gov/lightning/data/data_lis_iss.html) (Blakeslee, 2019). The second set of observations consist of the geostationary lightning data from the FY-4A LMI. Different from GLM's full-disk observation, LMI has two charge-coupled device (CCD) arrays, each with 400 × 300 pixels. The CCD arrays are capable of monitoring a half-hemisphere at a given time, as shown in Figure 1, with one observing the west side and another observing the east side, approximately between 70°E−150°E. From March to September, LMI observes the Northern Hemisphere, and the rest of the time, it monitors the Southern Hemisphere. The benefit of this approach is that LMI can observe local summer, when most of the lightning processes occur. More details about LMI can be found in the literature (Cao, 2016; Huang, 2007; Yang et al., 2017). In this study, we use 1-year of data collected from March 2017 to February 2018. The data processing details are given below.

In routine applications of LMI observations in weather monitoring, Level-2 lightning products, including the properties of lightning flashes, are used in the daily operation. As the input for the Level-2 clustering algorithms, the LMI Level-1 events are produced by the pre-process system and provide lightning event information, including the event time, location, pixel ID, event radiance, threshold radiance, and background radiance. To assess the ability of LMI in observing lightning, we use LMI Level-1 events in this study. These lightning events are saved on the server of the National Satellite Meteorological Centre (NSMC). The lightning event data occupy an extremely large storage space, which combined with a limited network

10.1029/2020EA001099

transmission speed, makes it difficult to download all of the Level-1 observations from the NSMC server. Therefore, in this study, a subset of LMI events was selected for detailed analysis. First, the ISS-LIS flash data that occurred during the LMI observation field-of-view were selected. Then, LMI events that occurred 1 min before or after any LIS flash time and in the whole LMI field-of-view were selected and downloaded from the NSMC server for further analysis.

3. Analyses of LMI Event Characteristics

3.1. Spatial Distribution

The geographical distribution of these extracted events between March 2017 and March 2018 is shown in Figure 1. In total, there are approximately 20.0 million and 3.3 million LMI events in the Northern Hemisphere and in the Southern Hemisphere, respectively. The four corners connected by the black solid lines in panels (a and b) are the designed corners of the LMI observation coverage. Inside the four corners, there are buffer regions, in which the number of LMI events increase gradually. Therefore, we chose four new corners inside the buffer regions. In the following discussion, only LMI events within the region boxed by dashed lines are used. In either hemisphere, the number of LMI events are summarized, respectively. Generally, the distribution patterns are consistent with the basic lightning climatology of LIS (Cecil et al., 2014). In China, the LMI event numbers gradually decrease from the coast to inland regions. In the Northern Hemisphere, the continental regions have a higher event frequency than the oceanic regions. The coastal regions also present a high frequency of LMI events, particularly along the long coast of eastern Asia. LMI is also able to capture events in lightning hot spots (Albrecht et al., 2016), such as Bangladesh and the Darwin region of Australia.

In Figure 1, the populations of LIS events in $2° \times 2°$ grids are shown in panels (c and d) and the ratios of LIS to LMI event numbers are shown in panels (e and f). As the ISS is a low-orbit platform, the total number of LIS events is much less than that of LMI events. In the mainland of China, the ratios of LIS to LMI events are generally less than 0.1. LIS observes a higher ratio of lightning events at high latitude and the edges of LMI's coverage. LMI shows less contrast between oceanic regions and continental regions. For example, the LMI events in the central Indian Ocean are comparable to those in the southern regions of Australia. This may be caused by insufficient consideration of the background radiances by LMI (see further details in following sections).

3.2. Diurnal Variation

With only half a year of observations in each hemisphere, the annual cycle or interannual variation in lightning activity cannot be examined at present. Here, we focus on the diurnal variation in lightning characteristics, which is crucial to lightning detection and a better understanding of the properties of thunderstorms. Figure 2a presents the diurnal variation in LMI events in both hemispheres. There are 13.8 and 2.6 million LMI events in the Northern Hemisphere and the Southern Hemisphere, respectively. After filtering events with event radiance less than 300 $\mu J\ sr^{-1}\ m^{-2}\ \mu m^{-1}$, the number of events decreases to 6.5 and 1.2 million, respectively. Note that only LMI events that occurred around the LIS flash time were downloaded from the NSMC server and analyzed here. The distributions show a distinct diurnal cycle with peaks around 1900 local solar time (LST) and low percentages around 0800 LST. The peaks in the afternoon are delayed compared to the typical distributions found by other lightning sensors (Liu & Zipser, 2008). Figure 2b shows the diurnal cycles of LIS observations in the LMI observation range; both the event data and group data were analyzed. In total, there are 1.9 million LIS events and 0.57 million LIS groups in the Northern Hemisphere, and 0.27 million events and 0.065 million groups in the Southern Hemisphere. Generally, the distribution peaks are located at 1500–1600 LST, with the exception of the diurnal cycle of the event data in the Southern Hemisphere. The discrepancies found between the event data and group data may be caused by a limited temporal range or different lightning characteristics between land and ocean.

There are many challenges to define LMI events, such as how to filter the pixels with low radiance and how to calculate the background radiance. For example, including LMI events with low radiances may lead to a large false alarm rate of flashes during the daytime and create an unrealistic diurnal cycle of lightning (Figure 2). To examine the impacts of low-radiance LMI events on the diurnal cycle, sensitivity experiments

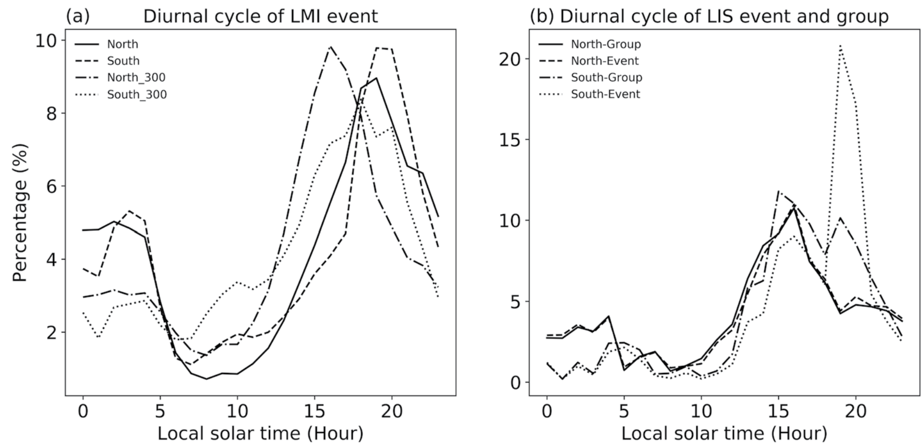

Figure 2. Diurnal variation in (a) Lightning Mapping Imager (LMI) events and (b) Lightning Imaging Sensor events and groups over the Northern Hemisphere and Southern Hemisphere. The number in the legend indicates that LMI events with an event radiance of less than 300 $\mu J\ sr^{-1}\ m^{-2}\ \mu m^{-1}$ are excluded.

were conducted with a simple radiance threshold to filter low-radiance LMI events. The results revealed that when the LMI events with event radiance less than 300 $\mu J\ sr^{-1}\ m^{-2}\ \mu m^{-1}$ are removed, the diurnal cycles of lighting events are close to the diurnal cycle variation of lightning shown by LIS in Figure 2b. From this perspective, the bias of the diurnal cycle in Figure 2a is possibly caused by over-filtering of low-radiance events in the daytime. Therefore, further improvements in processing low-radiance LMI events are also required, especially for lightning events during the daytime.

3.3. Lightning Radiance

The definitions of lightning events and subsequent processes of lightning products depend strongly on the background and threshold radiances at each pixel. To fully understand LMI's observational performance, the diurnal distributions of event radiance are presented in Figures 3 and 4. LMI events were investigated in different groups: All (all of the LMI events: 13.8/2.6 million LMI events for the Northern/Southern Hemisphere); Day (LMI events from 0900–1500 LST: 2.0/0.43 million); and Night (2100–0300 LST: 5.2/0.94 million). The Day and Night groups were analyzed separately, as the radiance at 777.4 nm is influenced significantly by solar radiance, particularly at sunrise and sunset. All the panels in Figure 3 reveal that the Day group has a larger event radiance and broader range than the Night group. The Night group shows a peak at around 200 $\mu J\ sr^{-1}\ m^{-2}\ \mu m^{-1}$, and the peak of the Day group is around 500 $\mu J\ sr^{-1}\ m^{-2}\ \mu m^{-1}$. Another feature is that the oceanic event radiance is smaller than the continental event radiance, especially during the daytime. The differences in event radiances between land and ocean during the nighttime are not as significant as during the daytime. Analysis of GLM has shown some similar results; that is, flash energy varies over oceanic regions and for a particular oceanic region, and the mean flash energy might be less than in the continental region (Koshak et al., 2018). However, in most studies, stronger flash energy is found over the ocean than the land from observations of TRMM-LIS (Chronis & Koshak, 2017), OTD (Beirle et al., 2014), and also GLM (Rudlosky, Goodman, Virts & Bruning, 2019). The discrepancy between this study and the generally accepted view implies that the distributions of radiance shown here are not robust and further investigation with an additional data set is needed. Overall, the results shown in Figure 3 suggest that the LMI preprocessing algorithm can still be improved to take into account these lands versus ocean differences.

The diurnal cycles of event radiance, background radiance, and threshold radiance are further detailed in Figure 4; radiance values at different percentiles are presented. The results are in line with distribution patterns obtained using theoretical values (Boccippio et al., 2002). In the Northern Hemisphere (left-hand panels in Figure 4), the three radiances are typical bell-shaped distributions, with peaks around 1200 LST. Among the three kinds of radiance, background radiance shows the largest contrast between daytime and nighttime and the smallest difference between the 25th and 90th percentiles. The background radiance

10.1029/2020EA001099

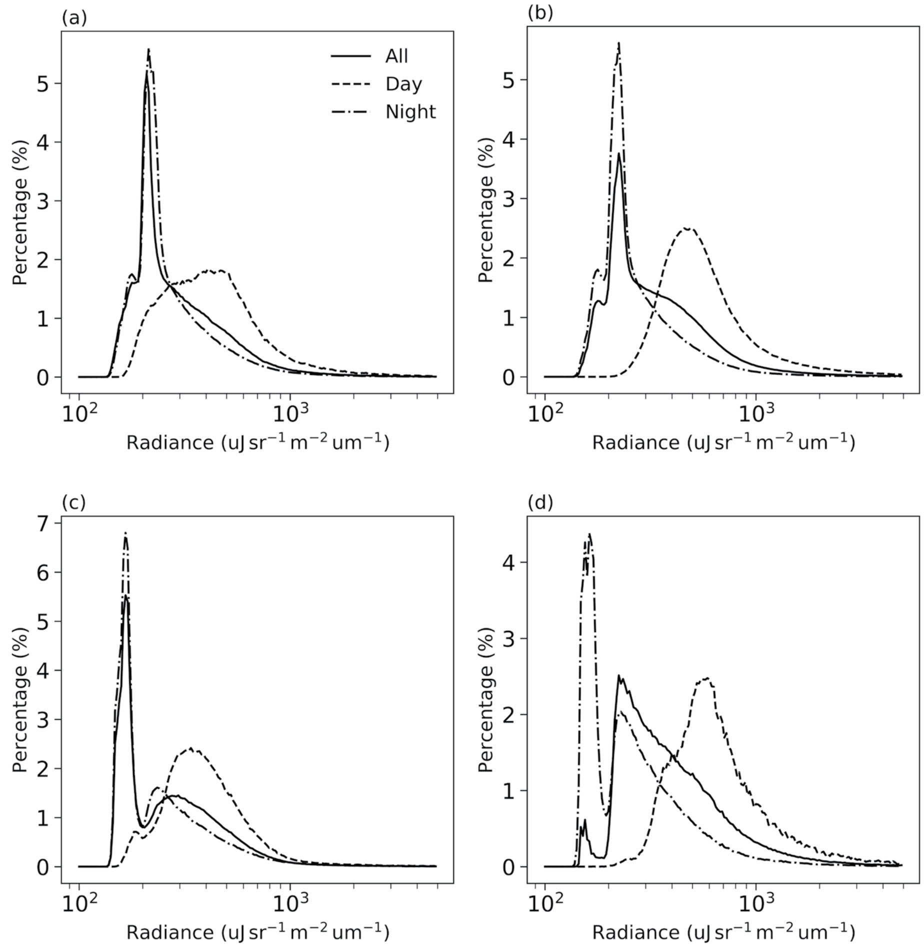

Figure 3. Probability distributions of Lightning Mapping Imager event radiance over (a) oceans of the Northern Hemisphere, (b) land of the Northern Hemisphere, (c) oceans of the Southern Hemisphere, and (d) land of the Southern Hemisphere. "All" indicates all the event radiance in the data set. "Day" ("Night") indicates event radiance from 09:00 local solar time (LST) (21:00 LST) to 15:00 LST (03:00 LST). The event radiance is the radiance exceedance over the background radiance.

ranges from less than 1,000 $\mu J\ sr^{-1}\ m^{-2}\ \mu m^{-1}$ at night to more than 10,000 $\mu J\ sr^{-1}\ m^{-2}\ \mu m^{-1}$ at noon. Moreover, the values of the event and background radiances show enormous differences. The background radiance at noon may be 10 times that of the event radiance. These large differences reveal the challenges in extracting the event radiance from the observed radiance. Note that only LMI events with an event radiance larger than 300 $\mu J\ sr^{-1}\ m^{-2}\ \mu m^{-1}$ are considered here. If the low-radiance events are considered, the difference between the event radiance and background radiance would be more noticeable. Although the results for the Northern Hemisphere are reasonable, those from the Southern Hemisphere (right-hand panels in Figure 4) are more complex. The three radiance types show peaks at around 1500 LST. The distribution of the event radiance in Figure 4b departs from a bell-shaped distribution and also shows a peak at around 1500 LST.

To examine the regional differences in radiance, the median values of radiance in a 2° × 2° box were calculated during the daytime over the Northern Hemisphere (Figure 5a) and over the Southern Hemisphere (Figure 5b). The most distinct feature is the contrast between continent and ocean, particularly in Figure 5b. The median values of the three radiance types are all smaller over the ocean than the continent. Over the land in the Northern Hemisphere, regional variation is evident. For example, northeastern China shows a large background radiance, which may be due to differences in the threshold of CCD sensitivity, land surface type, albedo, and so on. However, the spatial patterns of the three radiances also differ. The event

10.1029/2020EA001099

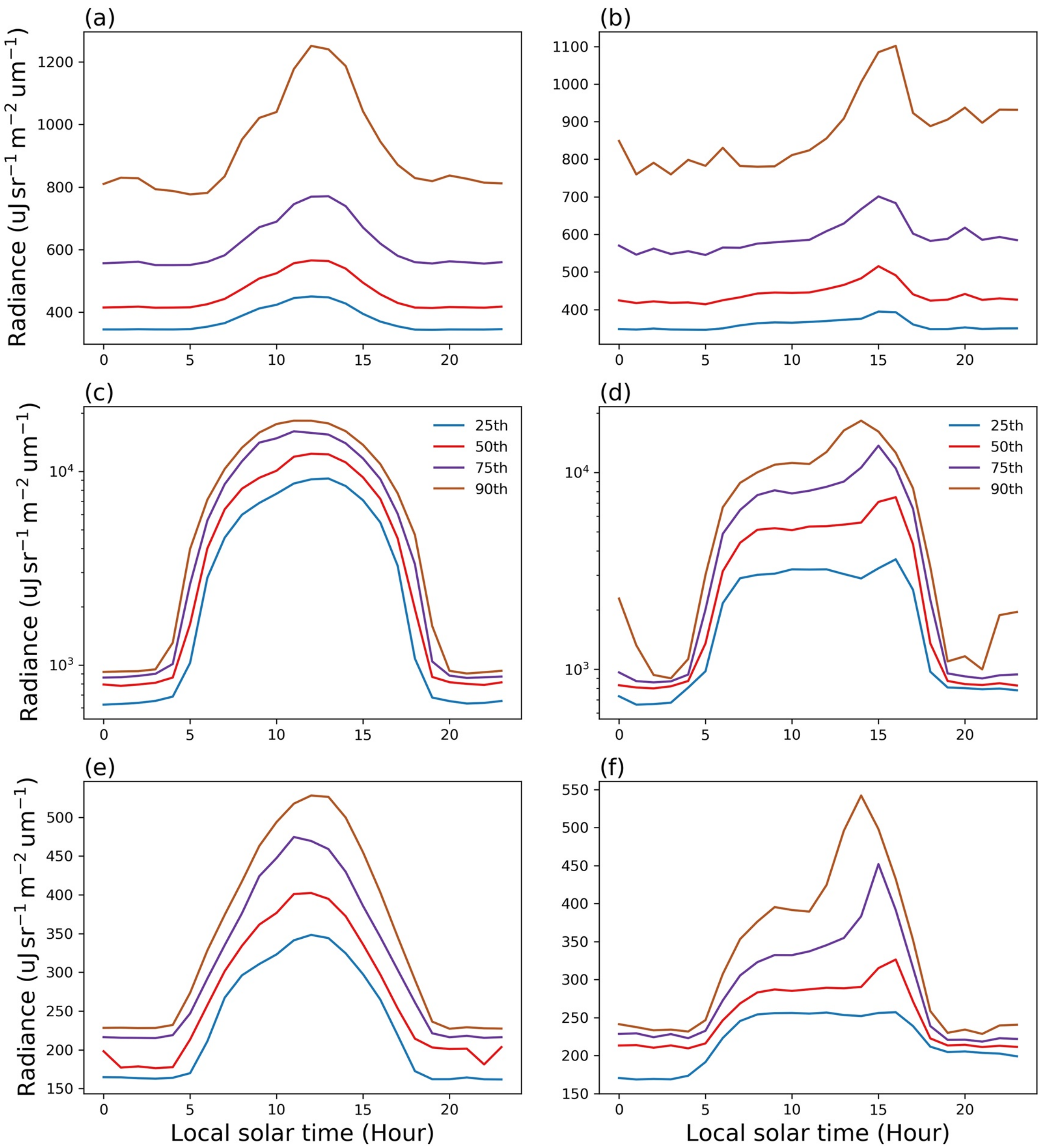

Figure 4. Diurnal distributions of the 25th, 50th, 75th, and 90th percentiles of the (a, b) Lightning Mapping Imager event radiance, (c, d) background radiance, and (e, f) threshold radiance over the Northern Hemisphere (a, c, e) and Southern Hemisphere (b, d, f).

radiance and threshold radiance tend to have higher values over the regions north of 35°N. In the Southern Hemisphere, the spatial patterns of the radiances over the ocean are also complex. The background radiance is smaller in the low-latitude region, which leads to higher event radiance in the low-latitude region. The event radiance during daytime is influenced by the solar radiance, which can be impacted by the incidence angle, cloud top, and so on. Therefore, regional differences in the event radiance may also be caused by the background. One possibility is insufficient consideration of the interaction between the incident radiance and cloud or the land surface. Nevertheless, this factor is difficult to assess at present.

The spatial distribution of radiance at nighttime is shown in Figure 6. The median values of the three kinds of radiance all show the feature that values are very close in adjacent grid boxes, resulting in the same color shading in adjacent grids. One possible explanation is the weak radiance at nighttime, as mentioned earlier. The radiance in the LMI Level-1 event data set we obtained has two digits. The two-digit number is then rescaled to a radiance value using the calibration coefficients, which vary at each CCD pixel and are derived

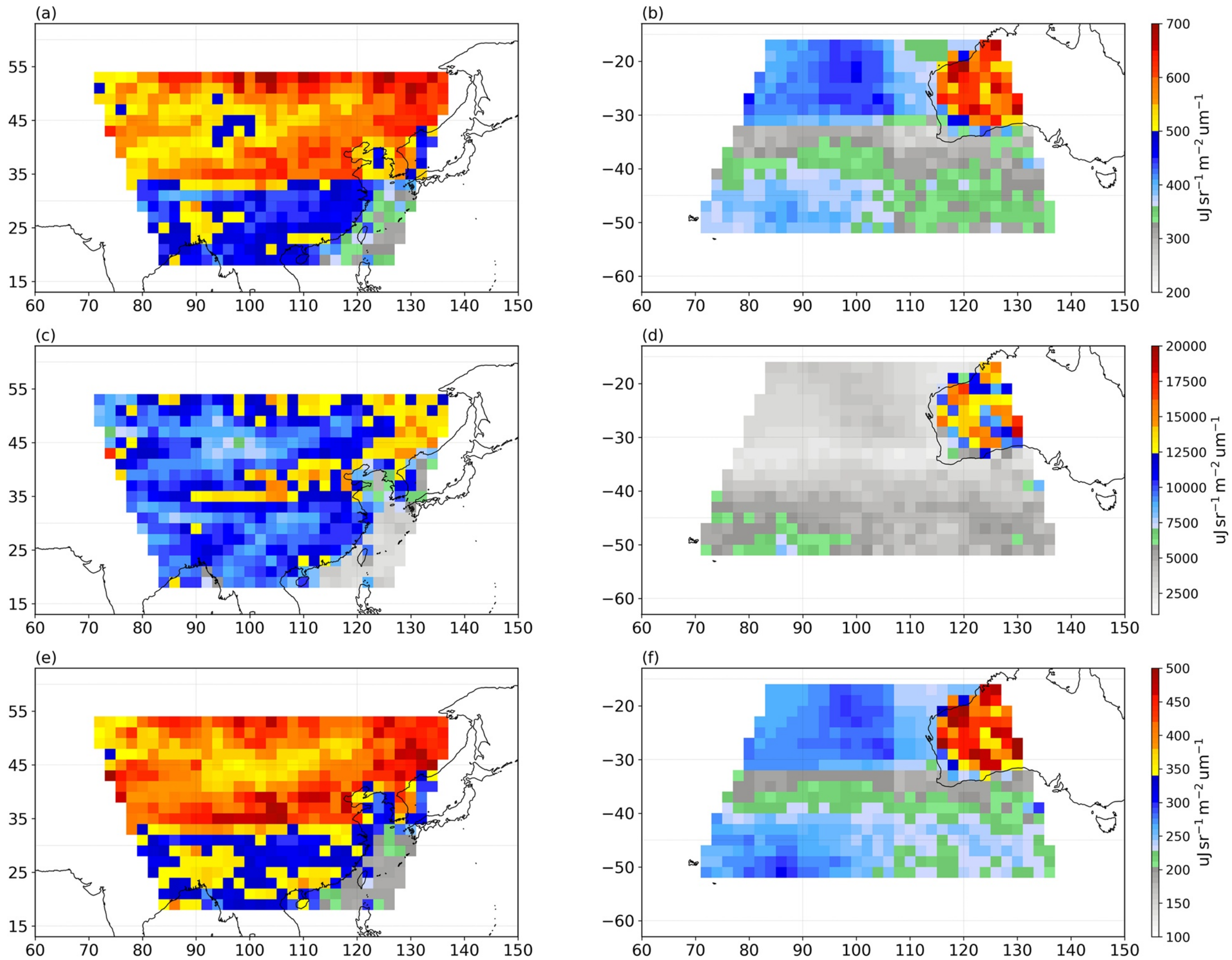

Figure 5. Median values of (a, b) event radiance, (c, d) background radiance, and (e, f) threshold radiance during the daytime from 09:00 local solar time (LST) to 15:00 LST over the Northern Hemisphere and Southern Hemisphere.

by the LMI's manufacturer. After the rescaling process, the radiance becomes difficult to recognize on the scale shown in Figure 6. The percentiles of event radiance at different LSTs are listed in Table 1. At 1200 LST, the event radiance at different percentiles is easy to distinguish, whereas at 2000 or 0200 LST, the event radiance changes very little before the 55th percentile. These results suggest that increasing the precision of the radiance values is required to promote further understanding of radiance, particularly low radiance. Moreover, the instrument bias is also believed to be significant during nighttime hours. For example, in Figures 6b–6e, significant differences are apparent between the west and east side fields of view, which indicates a difference in sensitivity between the two CCD arrays. Moreover, complex patterns of varying sensitivity across the CCD arrays are also obvious.

Overall, the radiance and the diurnal cycles of the LMI event frequency are closely related. At nighttime (2100 to 0300 LST), the lightning radiance is free from solar radiance interference. Therefore, a more accurate representation of the event radiance will be obtained at night when there are more low-radiance events. By contrast, the event radiance during the day is significantly influenced by the solar radiance and has much higher radiance values (Figure 3). In the algorithm of the space segment, pixels with a low radiance are not considered as lightning events, to exclude the noise caused by solar radiance. This creates artificial results in the LMI event's diurnal cycle. These deductions can be resolved with sensitivity runs, in which low-radiance events are excluded. Without considering low-radiance events, a higher percentage of LMI events at night are excluded, and the diurnal cycle of LMI events approaches a typical distribution (Figure 2a). This implies that the LMI algorithm excludes more low radiance events during the daytime than nighttime. Considering

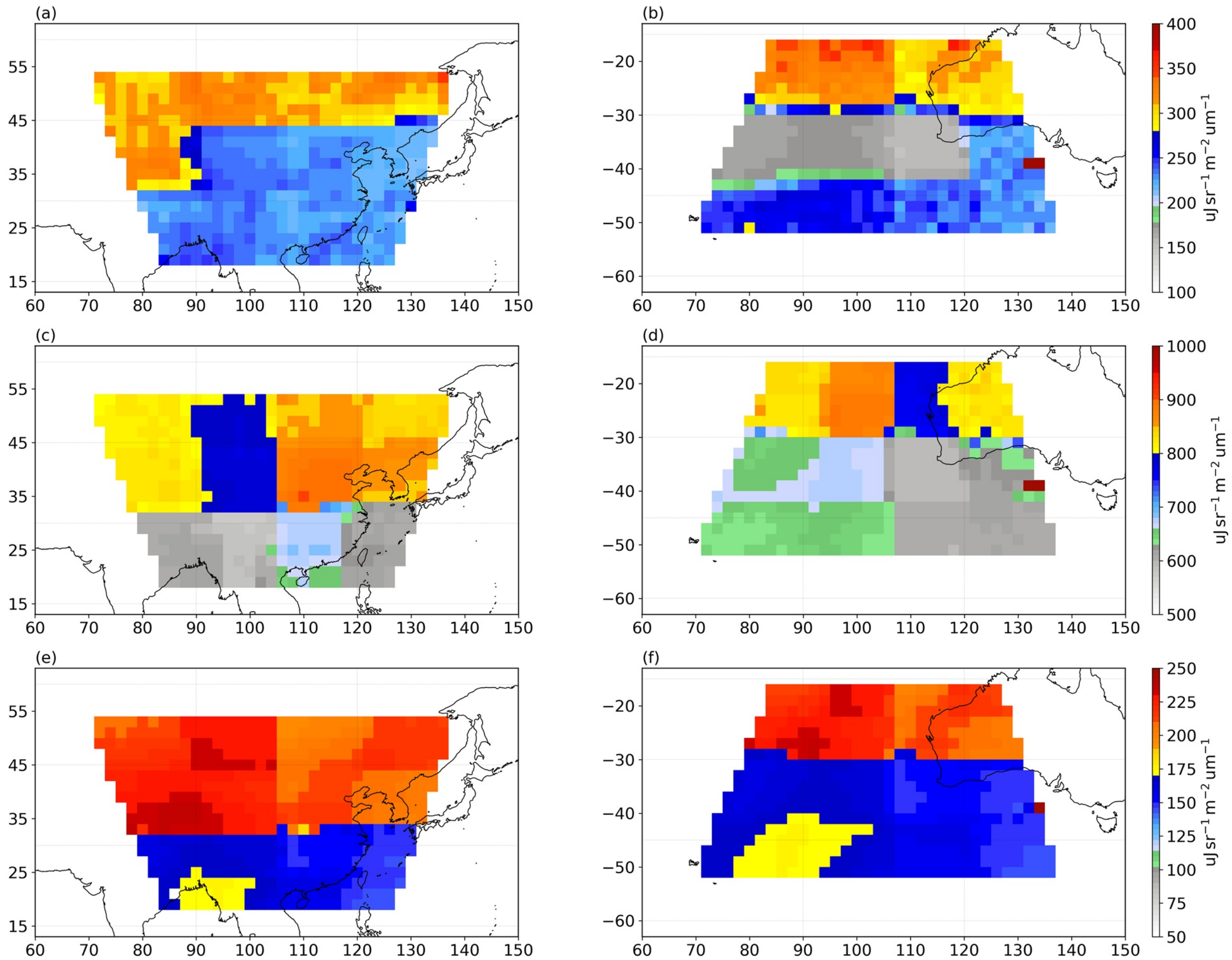

Figure 6. Similar to Figure 5 but for nighttime from 21:00 local solar time (LST) to 03:00 LST.

the less contamination from solar radiance during night time, the observed nighttime LMI events can be classified with a higher degree of confidence than the day-time ones. Thus, in the following analysis of the detection efficiency, all LMI events transmitted from the space segment are considered.

4. Assessment of LMI With LIS

In the examination of the LMI's performance, the group data of LIS observations were used to define the detection efficiency. The first step to assess LMI's performance was to match the LIS data with the LMI data. The LMI data used here were the event data. For the LIS data, we used the LIS group without considering the lightning's temporal evolution. For each LIS group, we searched the data set of LMI events that occurred within a certain temporal threshold (e.g., 1, 5, 10, 30, 50, 60 s) from the LIS group time, and over a certain spatial range (e.g., 0.2° or 0.5°) from the LIS group centroid location. Because of the coarse spatial and temporal matching thresholds, it was unlikely that we could depict the performance of LMI on an individual lightning detection and it is more likely to depict the detection of thunderstorms. For one LIS group, if one or more LMI events was matched, this LIS group was classified as a matched LIS group. Otherwise, the LIS group was considered to be a missing detection

Table 1
Percentiles of Event Radiance at Different Local Solar Time (LST)

Percentiles	20:00 LST	02:00 LST	12:00 LST
10^{th}	0.17	0.17	0.39
25^{th}	0.18	0.18	0.50
45^{th}	0.22	0.22	0.63
50^{th}	0.23	0.23	0.66
55^{th}	0.25	0.25	0.70
75^{th}	0.36	0.37	0.93
90^{th}	0.59	0.59	1.59

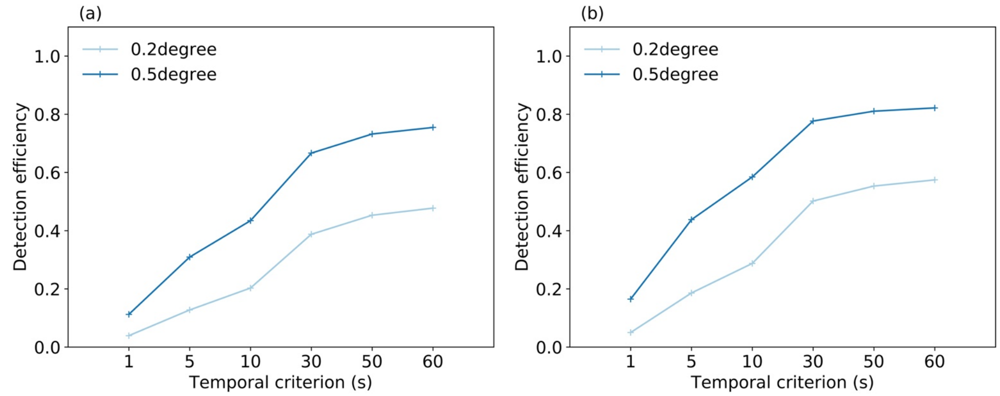

Figure 7. Summary of the detection efficiency relative to Lightning Imaging Sensor for different spatial and temporal criteria over the (a) Northern Hemisphere and (b) Southern Hemisphere.

by LMI. The LMI detection efficiency relative to LIS is defined by the matched LIS group number divided by the total LIS group number (DE = (matched LIS groups)/(total LIS groups)). Although continuous monitoring by LMI can be perceived as having the ability to detect all flash groups in LIS overpasses within the same observation region, in reality, this is not necessarily true. Because there is no perfect matching of the 2 ms observation time span between the two instruments, due to the nature of the short flash time of the lightning phenomenon, exact matching of an LMI event with an LIS group is actually difficult to achieve. Thus, the detection efficiency defined here only provides a reference for the chances of lightning flashes captured by both instruments simultaneously. For a lightning flash illuminating a large area, lasting a long time, and with large optical depth, for example, in organized convective systems, the chances of matching between the two would increase. However, for small thunderstorms with a low flash rate and a small cloud area, sparse lightning flashes are more challenging for both LIS and LMI.

The detection efficiency using different thresholds is summarized in Figure 7. Generally, it increases with the temporal threshold and the spatial threshold. For 0.5° and 60 s, the detection efficiency is close to 0.8, and the Southern Hemisphere is slightly larger than the Northern Hemisphere. The change between 10 and 30 s is larger than that between 5 and 10 s. Boccippio et al. (2000) showed that the time error distribution of OTD had a single peak at around 0 s. Recently, the timing accuracy of ISS-LIS was also found to be less than the native timing precision of the instrument itself (2 ms) (Blakeslee et al., 2020). These results imply that the tendency of the detection efficiency to increase should gradually slow down as the increase of temporal threshold. To check the fast increase in the detection efficiency between 10 and 30 s, the time error between the times of LMI and LIS was investigated over the Northern Hemisphere. The results (not shown here) revealed two peaks, distributed at around 0 s and −10 s. The lightning characteristics of these two peaks differed. For example, the diurnal cycle of the LMI event near −10 s was closer to a typical diurnal cycle distribution and with the stronger event radiance. However, with the present data, it is difficult to explain why the two peaks occurred; thus, we chose to leave this question open for further research with more observations and data. Notably, the fact that the LMI events matched with LIS groups does not necessarily mean that they are from the same lightning discharge process, given that the temporal threshold is far larger than the typical discharging process time. The detection efficiency is more likely to depict the possibility of LMI and LIS observing the same thunderstorm. It would be more relevant to determine the actual detection efficiency based on the data from available ground-based systems like the Lightning Mapping Array and compare these with what LMI "sees" in the future.

To match LMI and LIS, there are two crucial thresholds, namely the spatial and temporal thresholds. This section focuses on the LMI detection efficiency relative to LIS, with different combinations of spatial and temporal thresholds. First, the detection efficiency as a function of the area of the LIS group is shown in Figure 8. During the matching process of an LIS group to an LMI event, the centroid location of the LIS group was used. As the footprints of LIS and LMI differ, the spatial threshold must be larger than their footprints to match the two. In this case, the area of LIS would be a potential factor influencing the detection efficiency. The LIS event number in each group is considered to be the measurement of the LIS group area.

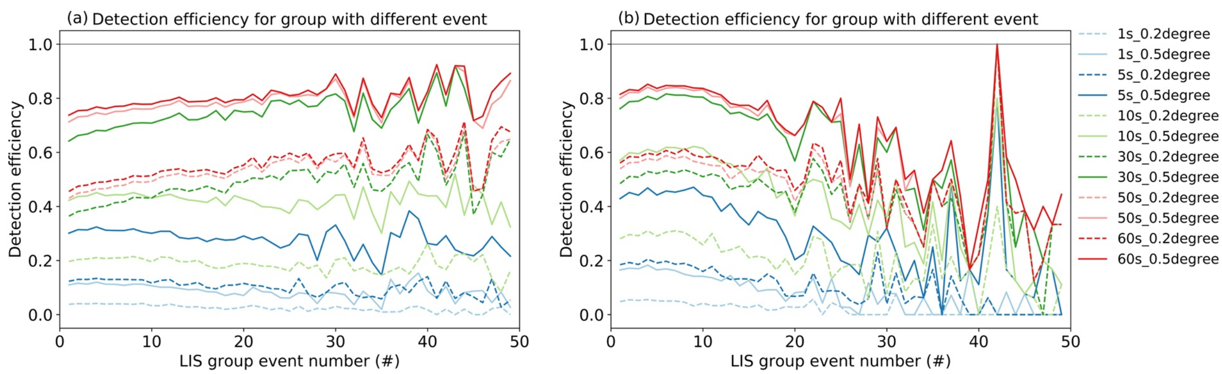

Figure 8. Relationship between the detection efficiency relative to Lightning Imaging Sensor (LIS) and the event numbers of the LIS groups over the (a) Northern Hemisphere and (b) Southern Hemisphere. The numbers in the legend indicate the temporal thresholds in seconds and the spatial thresholds in degrees.

In the Northern Hemisphere (Figure 8a), the detection efficiency changes with the temporal threshold. For temporal thresholds larger than 30 s, the detection efficiency increases with the LIS group area, with high variability for large-area LIS groups. However, for criteria with a temporal threshold of less than 10 s, the detection efficiency shows a slight reduction with the LIS group area. The relationship is more complex in the Southern Hemisphere (Figure 8b), where the detection efficiency decreases as the area of the LIS lightning group increases, with strong variability for large group areas. It is logical to speculate that the detection efficiency will increase with the group size of LIS because a greater area would be searched to match the LMI event. The opposite conclusion may be reached under limited sample numbers of LMI lightning events, particularly over the Southern Hemisphere.

Figures 9 and 10 show the spatial distribution of the detection efficiency over the Northern Hemisphere and the Southern Hemisphere, respectively. The space and time thresholds used are 0.5° and 60 s, respectively. Figures 9a and 9b show the LIS group number in each 2° grid box during the daytime (0900–1500 LST) and nighttime (2100–0300 LST). Regional differences are evident. For example, the lightning activity of the Tibetan Plateau is relatively weak and is more active in eastern China. Panels (c and d) show the matched LIS group, with similar spatial patterns. The detection efficiency is shown in the lower panels of Figure 9. The geographical distribution of detection efficiency presents a different pattern from the geographical distributions of an LIS group number. Unlike the LIS group number, the LMI detection efficiency relative to LIS over the northeast region is smaller than that over southern China during the daytime. One possible explanation is the matching difference between the two instruments for lightning with different durations and areas of illumination. LIS passes the high latitudes more frequently than the low latitudes, with a similar footprint resolution, whereas LMI monitors all regions with the same frequency but with a lower footprint resolution at the edges of the field of view. In the daytime, LMI's detection efficiency over the inland region, particularly the northwest region, is smaller than in the coastal region and this may be caused by the differences in convection or lightning over these two regions. The convection in the northwest region tends to be more isolated and smaller in size (Liu et al., 2008), and the matching process in this paper favors thunderstorms with higher flash rates. In the Southern Hemisphere (Figure 10), only the detection efficiency of LMI over land is presented due to the limited LIS sample size. Generally, the detection efficiency exceeds 0.8 in the portions of the Southern Hemisphere field of view.

The final characteristic of the detection efficiency discussed is the diurnal cycle, as shown in Figure 11. Over the Northern Hemisphere, the diurnal cycle of the LIS group number (Figure 11a) and matched LIS group number (Figure 11c) are both in line with a typical diurnal cycle of lightning activity. However, the diurnal cycle of the detection efficiency reveals a different phase, with lower values around noon and higher values during the nighttime. This feature is similar to the diurnal cycle of the predicted flash detection efficiency in the OTD data (Boccippio et al., 2000) and the observed LIS detection efficiency relative to GLM (Blakeslee et al., 2020). The main reason is due to solar radiance. This suggests that the radiance algorithm of LMI still requires further improvement, based on our comparison with LIS. In Figure 11b, the diurnal cycle is not as clear as presented in Figure 11a, due to the limited sample number, particularly at nighttime.

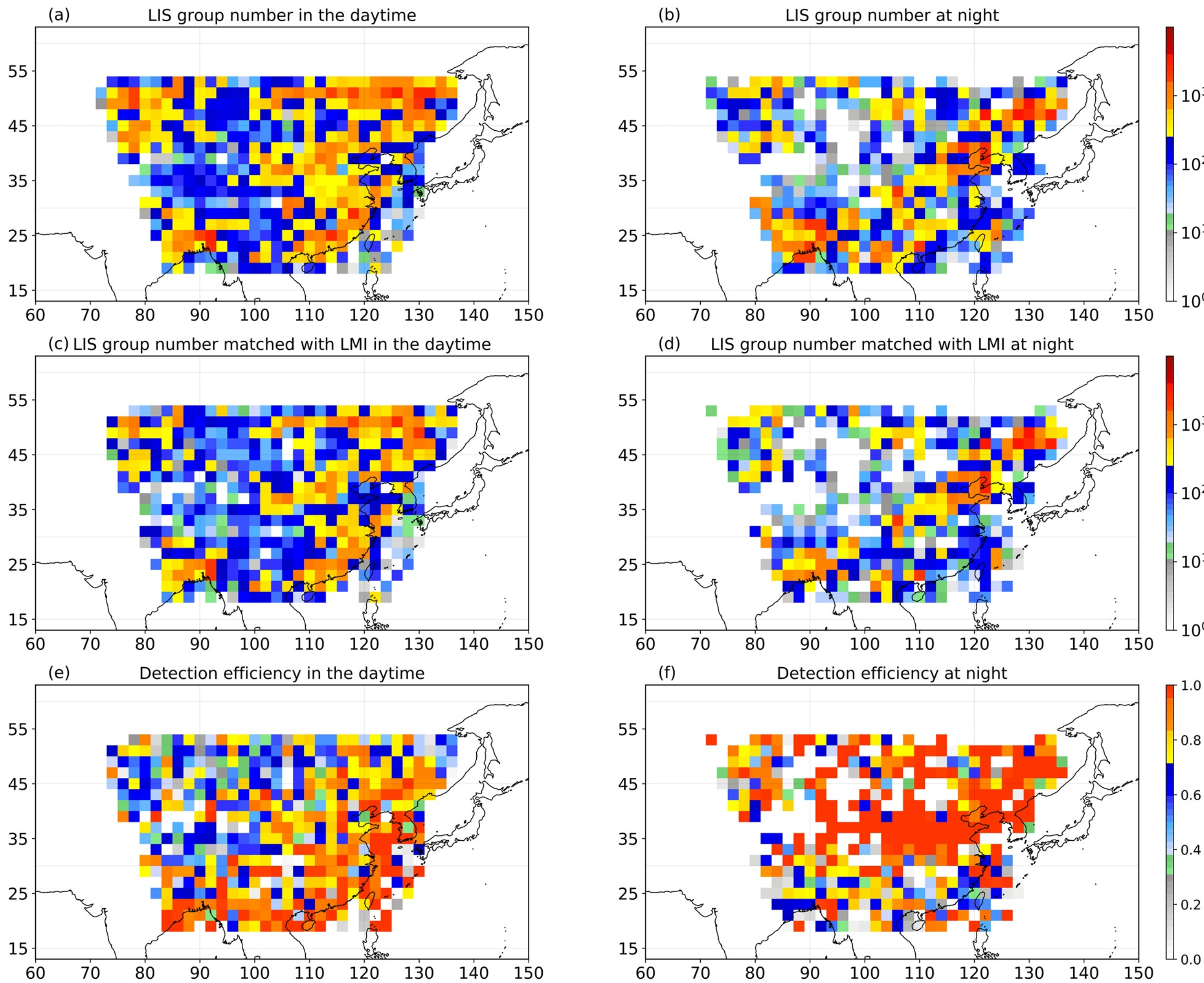

Figure 9. Total Lightning Imaging Sensor (LIS) group numbers in a 2° grid box over the Northern Hemisphere during (a) daytime and (b) nighttime. The matched LIS group numbers during (c) daytime and (d) nighttime. The detection efficiency relative to LIS during (e) daytime and (f) nighttime. Daytime is from 0900 to 1500 local solar time (LST) and nighttime is from 2100 to 0300 LST. The spatial and temporal thresholds are 0.5° and 60 s, respectively.

5. Conclusion and Discussion

With 1 year of LMI observations, the characteristics of selected LMI events were analyzed. Generally, LMI is able to capture the geographical distributions of lightning event frequency to certain extent, but the lack (or very small magnitude) of land–ocean contrast shown in Figures 1a and 1b is problematic. Over the oceans, LMI detects a higher fraction of events than LIS. The LMI Level-1 events show a shifted diurnal cycle toward the night, as compared to LIS′ results. From the radiance perspective, the radiance algorithm in the space segment may ignore a high percentage of low radiance events, especially in the daytime, due to solar radiance interference. After removing the LMI events with a radiance of less than 300 $\mu J\ sr^{-1}\ m^{-2}\ \mu m^{-1}$, the diurnal cycle of LMI events approached those of the LIS results. The detection efficiency based on the matching process against LIS groups revealed LMI's ability to detect thunderstorms on the assumption of relatively coarse thresholds (0.2° and 0.5° and 1, 5, 10, 30, 50, and 60 s). It seems like differences in the instrument or algorithm sensitivity are more likely to cause decreased detection efficiency values near noon, especially given there is no reason to expect flashes with short duration and small illumination areas to occur preferentially near noon. The spatial distribution also revealed regional differences in the detection efficiency over mainland China.

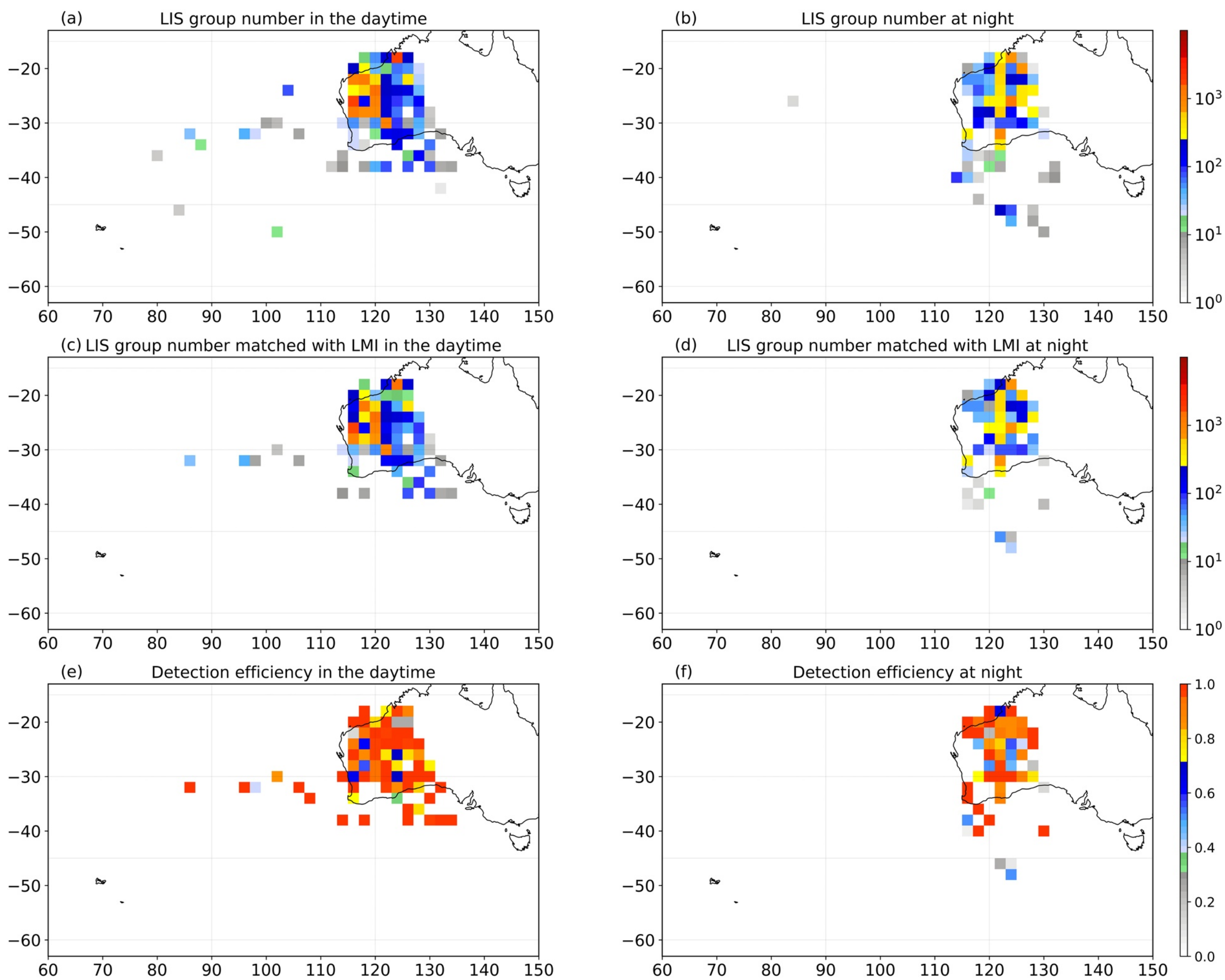

Figure 10. Similar to Figure 9 but for the Southern Hemisphere.

In this study, only LMI events that occurred 1 min prior to or after the LIS flash time were considered. Although the number of these selected LMI event samples is still considerable, the statistical results may be biased. Meanwhile, 1 year of observational results is not sufficient to draw robust conclusions on a high spatial resolution grid, particularly when there is only a half-year of observation for each hemisphere. Further investigation of LMI's observations requires a more complete collection of LMI events. However, as discussed before, the main cause of the shifted diurnal cycle is from over-filtering of low-radiance events during the daytime, which suggests a better algorithm for background radiance estimation is needed. Nevertheless, the LMI lightning algorithm continues to be updated, which will provide a better algorithm for LMI event definition in future products. Further, the event radiances play a key role not only in LMI's performance, but also as a parameter to facilitate convection studies.

In the assessment of LMI's performance using LIS, the temporal and spatial resolutions of both instruments were found to still be too coarse to be regarded as a real cross-comparison. Many factors could contribute to the uncertainties in the direct collocation of two products. The differences in resolutions and orbit altitudes between LMI and LIS could have significant influences on the validation process. Cross validations using multiple lightning observations found that the GLM detection efficiency could be low as 20% when the flash channel length is less than 5 km and could reach 80% if the channel length is longer than 30 km (Zhang & Cummins, 2019). Meanwhile, an examination of the event numbers in TRMM-LIS groups showed that almost half of the groups only had one or two events (Zhang & Cummins, 2019). These results explain the poor detection of short duration flashes of GLM and also help to interpret LMI's performance and

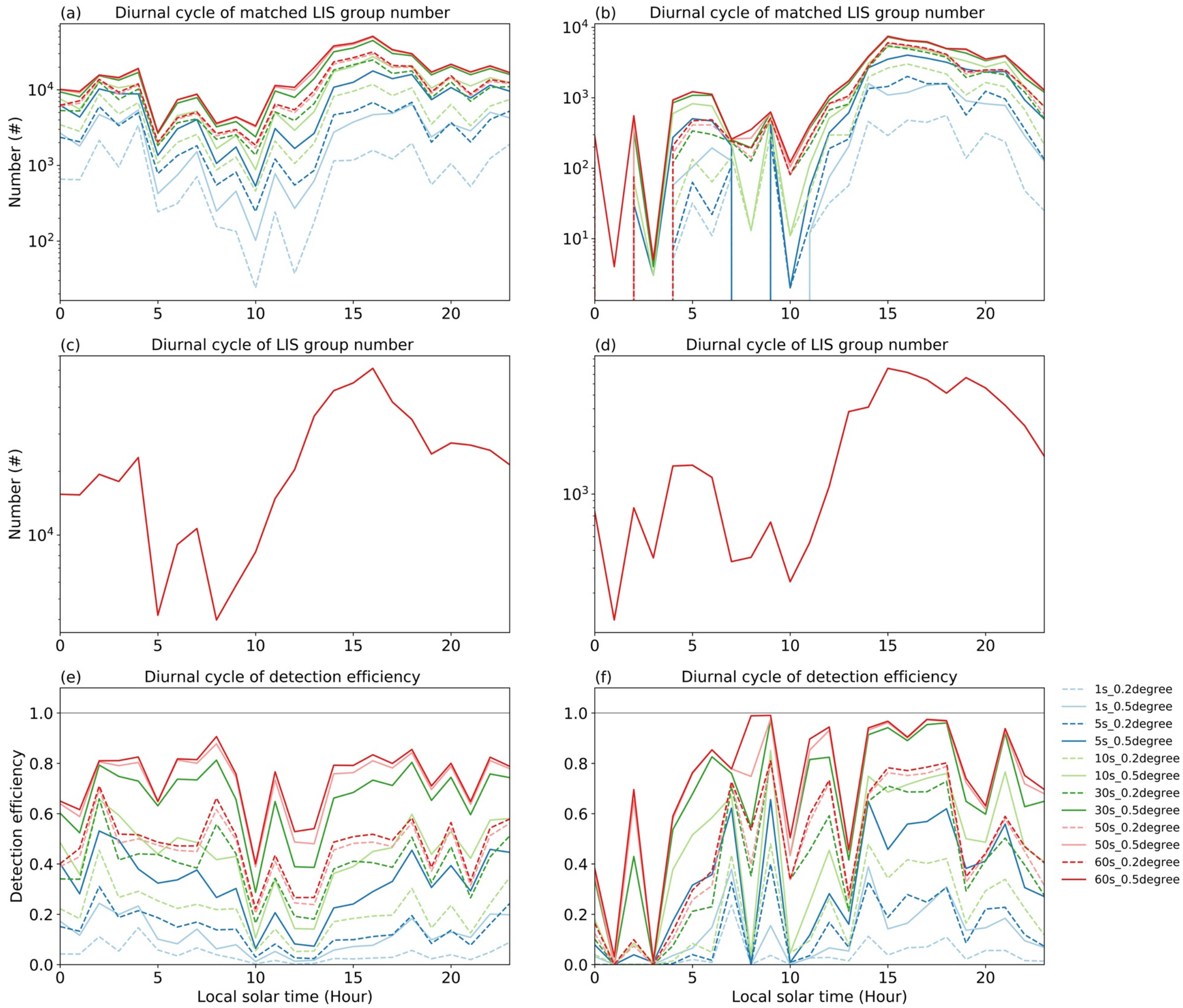

Figure 11. Diurnal variation in the population of matched Lightning Imaging Sensor (LIS) groups, total LIS groups, and the detection efficiency relative to LIS over the Northern Hemisphere (a, c, e) and Southern Hemisphere (b, d, f).

the results shown here. For example, low detection efficiency is found over the Tibetan Plateau, where convection is typically small in size and likely to involve short-duration flashes that are difficult for LMI to capture. The collocated LMI events and LIS groups are not necessarily from the same discharging process, because the matching thresholds used here are much coarser; therefore, they are more likely matches of different discharges in the same thunderstorm or thunderstorm complex. Nevertheless, as the temporal scale of thunderstorms ranges from dozens of minutes to several hours, the LMI event number is still of helpful information in the study of storm-related phenomena. For example, a maximum lightning frequency observed by FY-4A occurred 45 min before the maximum rain rate during a heavy rain process in Xiamen, a coastal city in southeastern China (Zhang et al., 2019).

As the two GLM sensors in the Western Hemisphere are also in routine operation and MTG-LI and LMI onboard FY-4C are being planned, similar research should be conducted between GLM/LI/LMI and ISS-LIS in future to validate their performances, which would also serve to facilitate a comparison of these multiple sensors, improve our understanding of lightning observation from geostationary satellites, and expand research into thunderstorm and severe weather events using the lightning data. Apart from the cross-validation of low-orbit lightning and geostationary lightning, it is also important to apply geostationary lightning observations with other instruments, such as the Dual-frequency Precipitation Radar onboard the global precipitation measurements (GPM) core satellite. The geostationary lightning sensor would provide continual monitoring of convection, which can be combined with the three-dimensional imaging capabilities of the GPM to gain insight into the evolution of convection, particularly in regions without a sufficient ground radar network.

Data Availability Statement

The LIS data used in this manuscript are available on the website (https://ghrc.nsstc.nasa.gov/lightning/data/data_lis_iss.html). Due the data policy of NSMC, it is not permitted to personally make the LMI Level-1 data openly available. The readers could contact the NSMC to obtain the data set. Meanwhile, the data used to plot the figures are open on the Baidu Cloud (https://pan.baidu.com/s/1tM2Yf08ElNwGPk1ToPv2Mg).

Acknowledgments

The study was supported by the National Natural Science Foundation of China grant No. 42030607. X. N. is also supported by the Grants for Chongqing's Scholars with Overseas Experience (cx2019042) and Supported by Key Laboratory of Tropical Atmosphere-Ocean System (Sun Yat-sen University), Ministry of Education. The authors thank the editor and anonymous reviewers, whose valuable comments and suggestions significantly improved this article.

References

Albrecht, R. I., Goodman, S. J., Buechler, D. E., Blakeslee, R. J., & Christian, H. J. (2016). Where are the lightning hotspots on earth? *Bulletin of the American Meteorological Society*, *97*, 2051–2068. https://doi.org/10.1175/BAMS-D-14-00193.1

Bateman, M., & Mach, D. (2020). Preliminary detection efficiency and false alarm rate assessment of the Geostationary Lightning Mapper on the GOES-16 satellite. *Journal of Applied Remote Sensing*, *14*. https://doi.org/10.1117/1.JRS.14.032406

Beirle, S., Koshak, W., Blakeslee, R., & Wagner, T. (2014). Global patterns of lightning properties derived by OTD and LIS. *Natural Hazards and Earth System Sciences*, *14*, 2715–2726. https://doi.org/10.5194/nhess-14-2715-2014

Blakeslee, R. (2019). *Non-quality controlled Lightning Imaging Sensor (LIS) on International Space Station (ISS) science data*. NASA Global Hydrology Resource Center DAAC. https://doi.org/10.5067/LIS/ISSLIS/DATA107

Blakeslee, R., & Koshak, W. (2016). LIS on ISS: Expanded global coverage and enhanced applications. *The Earth Observer*, *28*, 4–14.

Blakeslee, R. J., Lang, T. J., Koshak, W. J., Buechler, D., Gatlin, P., Mach, D. M., et al. (2020). Three years of the Lightning Imaging Sensor onboard the International Space Station: Expanded global coverage and enhanced applications. *Journal of Geophysical Research: Atmospheres*, *125*(16), e2020JD032918. https://doi.org/10.1029/2020JD032918

Boccippio, D. J., Koshak, W., Blakeslee, R., Driscoll, K., Mach, D., Buechler, D., et al. (2000). The Optical Transient Detector (OTD): Instrument characteristics and cross-sensor validation. *Journal of Atmospheric and Oceanic Technology*, *17*, 441–458. https://doi.org/10.1175/1520-0426(2000)017<0441:TOTDOI>2.0.CO;2

Boccippio, D. J., Koshak, W. J., & Blakeslee, R. J. (2002). Performance assessment of the optical transient detector and lightning imaging sensor. Part I: Predicted diurnal variability. *Journal of Atmospheric and Oceanic Technology*, *19*, 1318–1332. https://doi.org/10.1175/1520-0426(2002)019<1318:paotot>2.0.co;2

Buechler, D., Varghese, T., Armstrong, P., Bremer, J., & Lamb, R. (2018). *On-orbit validation of the Geolocation Accuracy of the GOES-16 Geostationary Lightning Mapper (GLM) Flashes using Ground-based Laser Beacons* (pp. 1–8).

Buechler, D. E., Blakeslee, R. J., Cecil, D. J., & Koshak, W. J. (2019). Initial results from the Lightning Imaging (LIS) on the International Space Station (ISS) and comparison with observations from the Tropical Rainfall Measuring Mission (TRMM) LIS. In Ninth Conference on the Meteorological Application of Lightning Data (Vol. 1).

Cao, D. (2016). The development of product algorithm of the Fengyun-4 geostationary Lightning Mapping Imager. *Advances in Meteorological Science and Technology*, *6*, 94–98. https://doi.org/10.3969/j.issn.2095-1973.2016.01.014

Cao, D., Lu, F., Zhang, X., & Zhang, Z. (2018). Applications of FY4 lightning observation product on monitoring severe weather. *Satellite Applications*, *11*, 18–23.

Cecil, D. J., Buechler, D. E., & Blakeslee, R. J. (2014). Gridded lightning climatology from TRMM-LIS and OTD: Dataset description. *Atmospheric Research*, *135-136*, 404–414. https://doi.org/10.1016/j.atmosres.2012.06.028

Cecil, D. J., Goodman, S. J., Boccippio, D. J., Zipser, E. J., & Nesbitt, S. W. (2005). Three years of TRMM precipitation features. Part I: Radar, radiometric, and lightning characteristics. *Monthly Weather Review*, *133*, 543–566. https://doi.org/10.1175/MWR-2876.1

Christian, H. J., Blakeslee, R. J., Boccippio, D. J., Boeck, W. L., Buechler, D., Driscoll, K. T., et al. (2003). Global frequency and distribution of lightning as observed from space by the Optical Transient Detector. *Journal of Geophysical Research*, *108*(D1). https://doi.org/10.1029/2002JD002347

Christian, H. J., Blakeslee, R. J., & Goodman, S. J. (1989). The detection of lightning from geostationary orbit. *Journal of Geophysical Research*, *94*(D11), 13329–12337. https://doi.org/10.1029/jd094id11p13329

Chronis, T., & Koshak, W. J. (2017). Diurnal variation of TRMM/LIS Lightning flash radiances. *Bulletin of the American Meteorological Society*, *98*, 1453–1470. https://doi.org/10.1175/BAMS-D-16-0041.1

Curtis, N., Carey, L. D., & Schultz, C. (2018). An Analysis of the Lightning Jump Algorithm Using Geostationary Lightning Mapper Flashes. In *25th International Lightning Detection Conference & 7th International Lightning Meteorology Conference* (pp. 1–6).

Dobber, M., & Kox, S. (2016). Meteosat Third Generation (MTG) Lightning Imager (LI) calibration and 0-1b data processing. In *25th CALCON Techinical Meeting* (pp. 1–13).

Farnell, C., Rigo, T., & Pineda, N. (2017). Lightning jump as a nowcast predictor: Application to severe weather events in Catalonia. *Atmospheric Research*, *183*, 130–141. https://doi.org/10.1016/j.atmosres.2016.08.021

Fierro, A. O., Stevenson, S. N., & Rabin, R. M. (2018). Evolution of GLM-observed total lightning in Hurricane Maria (2017) during the period of maximum intensity. *Monthly Weather Review*, *146*, 1641–1666. https://doi.org/10.1175/MWR-D-18-0066.1

Fierro, A. O., Wang, Y., Gao, J., & Mansell, E. R. (2019). Variational assimilation of radar data and GLM lightning-derived water vapor for the short-term forecasts of high-impact convective events. *Monthly Weather Review*, *147*, 4045–4069. https://doi.org/10.1175/MWR-D-18-0421.1

Goodman, S., Mach, D., Koshak, W., & Blakeslee, R. (2012). *Algorithm theoretical basic document—GLM lightning cluster filter algorithm*.

Goodman, S. J., Blakeslee, R., Koshak, W. J., Mach, D., Bailey, J., Buechler, D., et al. (2013). The GOES-R Geostationary Lightning Mapper (GLM). *Atmospheric Research*, *125–126*, 34–49. https://doi.org/10.1016/j.atmosres.2013.01.006

Hu, J., Rosenfeld, D., Ryzhkov, A., & Zhang, P. (2020). Synergetic use of the wsr-88d radars, goes-r satellites, and lightning networks to study microphysical characteristics of hurricanes. *Journal of Applied Meteorology and Climatology*, *59*, 1051–1068. https://doi.org/10.1175/JAMC-D-19-0122.1

Huang, F. (2007). The goal and challenge of Lightning Mapping Imager of FY-4. *Meteorological Science and Technology*, *35*, 35–42. https://doi.org/10.15258/sst.2007.35.3

Kong, R., Xue, M., Fierro, A. O., Jung, Y., Liu, C., Mansell, E. R., & Macgorman, D. R. (2020). Assimilation of GOES-R geostationary lightning mapper flash extent density data in GSI ENKF for the analysis and short-term forecast of a mesoscale convective system. *Monthly Weather Review*, *148*(5), 2111–2133. https://doi.org/10.1175/MWR-D-19-0192.1

Koshak, W., Bitzer, P., & Goodman, S. (2018). Flash optical energy from the Geostationary Lightning Mapper. In *XVI International Conference on Atmospheric Electricity* (pp. 1–9).

Kummerow, C., Barnes, W., Kozu, T., Shiue, J., & Simpson, J. (1998). The Tropical Rainfall Measuring Mission (TRMM) sensor package. *Journal of Atmospheric and Oceanic Technology*, *15*, 809–817. https://doi.org/10.1016/0273-1177(94)90210-0

Liang, H., Bao, S., Chen, Q., Zhao, X., & Li, Y. (2017). Design and implementation of FY-4 Geostationary Lightning Imager. *Aerospace Shanghai*, *34*, 43–51. https://doi.org/10.19328/j.cnki.l006-1630.2017.04.006

Liu, C., Cecil, D. J., Zipser, E. J., Kronfeld, K., & Robertson, R. (2012). Relationships between lightning flash rates and radar reflectivity vertical structures in thunderstorms over the tropics and subtropics. *Journal of Geophysical Research: Atmospheres*, *117*(D6). https://doi.org/10.1029/2011JD017123

Liu, C., & Zipser, E. J. (2008). Diurnal cycles of precipitation, clouds, and lightning in the tropics from 9 years of TRMM observations. *Geophysical Research Letters*, *35*(4), 1–6. https://doi.org/10.1029/2007GL032437

Liu, C., Zipser, E. J., Cecil, D. J., Nesbitt, S. W., & Sherwood, S. (2008). A cloud and precipitation feature database from nine years of TRMM observations. *Journal of Applied Meteorology and Climatology*, *47*, 2712–2728. https://doi.org/10.1175/2008JAMC1890.1

Liu, Y., Li, Z., & Wang, H. (2019). *Comparison and analysis of lightning occurrence characteristics based on data obtained by Fengyun-4A satellite and ADTD three-dimensional lightning monitoring network in Jiangsu Province*. IEEE.

MacGorman, D. R., Burgess, D. W., Mazur, V., & Rust, W. D. (1988). Lightning rates relative to tornadic storm evolution on 22 May 1981. *Journal of the Atmospheric Sciences*, *46*(2), 221–251. https://doi.org/10.1175/1520-0469(1989)046<0221:lrrtts>2.0.co;2

NOAA-NASA. (2019). *GOES-R Series Data Book* (p. 240). Retrieved from https://www.goes-r.gov/downloads/resources/documents/GOES-RSeriesDataBook.pdf

Orville, R. E., & Henderson, R. W. (1986). Global distribution of midnight lightning: September 1977 to August 1978. *Monthly Weather Review*, *114*, 2640–2653. https://doi.org/10.1175/1520-0493(1986)114<2640:GDOMLS>2.0.CO;2

Padula, F., Goodman, S. J., Pearlman, A., Cao, C., Llc, G., Nesdis, N., et al. (2017). Advanced Baseline Imager (ABI) and Geostationary Lightning Mapper (GLM) calibration/validation from a field campaign perspective. In *2017 IEEE International Geoscience and Remote Sensing Symposium (IGARSS)* (pp. 301–304).

Petersen, W. A., Christian, H. J., & Rutledge, S. A. (2005). TRMM observations of the global relationship between ice water content and lightning. *Geophysical Research Letters*, *32*(14), 1–4. https://doi.org/10.1029/2005gl023236

Rudlosky, S. D., Goodman, S. J., & Virts, K. S. (2019). *Lightning detection: GOES-R Series Geostationary Lightning Mapper: Lightning Detection: GOES-R Series Geostationary Lightning Mapper* (pp. 193–202). Elsevier Inc. https://doi.org/10.1016/B978-0-12-814327-8.00016-0

Rudlosky, S. D., Goodman, S. J., Virts, K. S., & Bruning, E. C. (2019). Initial Geostationary Lightning Mapper observations. *Geophysical Research Letters*, *46*, 1097–1104. https://doi.org/10.1029/2018GL081052

Schultz, C. J., Petersen, W. A., & Carey, L. D. (2009). Preliminary development and evaluation of lightning jump algorithms for the real-time detection of severe weather. *Journal of Applied Meteorology and Climatology*, *48*, 2543–2563. https://doi.org/10.1175/2009JAMC2237.1

Thompson, K. B., Bateman, M. G., & Carey, L. D. (2014). A comparison of two ground-based lightning detection networks against the Satellite-Based Lightning Imaging Sensor (LIS). *Journal of Atmospheric and Oceanic Technology*, *31*(10), 2191–2205. https://doi.org/10.1175/jtech-d-13-00186.1

Williams, E., Boldi, B., Matlin, A., Weber, M., Hodanish, S., Sharp, D., et al. (1999). The behavior of total lightning activity in severe Florida thunderstorms. *Atmospheric Research*, *51*, 245–265. https://doi.org/10.1016/S0169-8095(99)00011-3

Yang, J., Zhang, Z., Wei, C., Lu, F., & Guo, Q. (2017). Introduction the new generation of Chinese geostationary weather satellites, Fengyun-4. *Bulletin of the American Meteorological Society*, *98*(8), 1637–1658. https://doi.org/10.1175/BAMS-D-16-0065.1

Zhang, D., & Cummins, K. L. (2019). Ground and space-based observations of horizontally extensive lightning flashes. In *Ninth Conference on the Meteorological Application of Lightning Data* (pp. 1–6).

Zhang, D., & Cummins, K. L. (2020). Time evolution of satellite-based optical properties in lightning flashes, and its impact on GLM flash detection. *Journal of Geophysical Research : Atmospheres*, *125*(6), https://doi.org/10.1029/2019JD032024

Zhang, X., Wei, M., & Pan, J. (2019). Application of FY-4 lightning data in monitoring and warning a heary precipitation in Xiamen on May 7, 2018. *Remote Sensing Technological Applications*, *34*, 1082–1090. https://doi.org/10.11873/j.issn.1004/0323.2019.5.1082